

# Numerical simulation of the head-on collision of two equal-sized drops with van der Waals forces

X. Jiang · A. J. James

Received: 04 February 2006 / Accepted: 22 August 2006 / Published online: 10 November 2006  
© Springer Science+Business Media B.V. 2006

**Abstract** The head-on collision of two equal-sized drops in a hyperbolic flow is investigated numerically. An axisymmetric volume-of-fluid (VOF) method is used to simulate the motion of each drop toward a symmetry plane where it interacts and possibly coalesces with its mirror image. The volume-fraction boundary condition on the symmetry plane is manipulated to numerically control coalescence. Two new numerical methods have been developed to incorporate the van der Waals forces in the Navier–Stokes equations. One method employs a body force computed as the negative gradient of the van der Waals potential. The second method employs the van der Waals forces in terms of a disjoining pressure in the film depending on the film thickness. Results are compared to theory of thin-film rupture. Comparisons of the results obtained by the two methods at various values of the Hamaker constant show that the van der Waals forces calculated from the two methods have qualitatively similar effects on coalescence. A study of the influence of the van der Waals forces on the evolution and rupture of the film separating the drops reveals that the film thins faster under stronger van der Waals forces. Strong van der Waals forces lead to nose rupture, and small van der Waals forces lead to rim rupture. Increasing the Reynolds number causes a greater drop deformation and faster film drainage. Increasing the viscosity ratio slows film drainage, although the effect is small for small viscosity ratio.

**Keywords** Drop collision · Coalescence · Van der Waals force · Volume of fluid

## 1 Introduction

Drop collision is encountered in a wide range of processes. Rain-drop formation is one example from nature. Numerous applications involving drop collisions can also be found in industry. In polymer blending, coalescence and break-up of liquid particles govern the development of the blend's morphology which determines the physical properties of the blend. In spray combustion, frequent collisions of drops in the dense spray region near the injector can significantly affect drop size and velocity, and thus the

---

X. Jiang · A. J. James (✉)  
Department of Aerospace Engineering and Mechanics, University of Minnesota, Minneapolis, MN, 55455, USA  
e-mail: ajames@aem.umn.edu

X. Jiang  
e-mail: xljiang@aem.umn.edu

ultimate combustion performance. Examples of drop collision also abound in various other fields, such as liquid–liquid extraction, ink-jet printing, drug delivery, and waste treatment.

Due to its significance, drop collision has been of interest to researchers for decades. However, most studies have been limited to experiments because of the complex physics and the wide range of length scales in this process. The literature on experimental investigations of collision problems is extensive. According to previous studies (1), binary collision outcomes can be generally divided into four regimes: bouncing, in which two drops collide and bounce apart; coalescence, in which two drops merge permanently forming a single drop; separation, in which drops coalesce temporarily and then split into two drops again; and fragmentation, in which small satellite drops are formed during separation of the temporarily coalesced drops.

Many efforts have been made to understand the characteristics of different collision behaviors, the boundaries separating them, and the physics behind them. Ashgriz and Poo (2) conducted extensive experiments on coalescence and separation collisions. The regimes of coalescence and two different types of separation characterized by the impact parameter, namely reflexive separation for small impact parameters and stretching separation for large impact parameters, were found in the space of Weber number and impact parameter. A systematic experimental study of collision dynamics of equal-sized water and hydrocarbon drops was performed by Jiang et al. (3). Boundaries between different collision outcomes for five different hydrocarbons were delineated, showing significant differences from those of water drops. Energy dissipation during the collision process, as well as the effects of the material properties of the fluids on collision behaviors, were also analyzed. Qian and Law (4) extended Jiang's study and investigated the effects of the ambient gas, including gas pressure, viscosity, molecular weight, and molecular structure, on the transition between different collision regimes. Qian and Law (4) also presented a coalescence/separation criterion for head-on collisions. A review of experimental studies of water and fuel-drop collision dynamics in quiescent air can be found in (1). Motivated by the importance of flow-induced coalescence in polymer blending and other applications, Leal and co-workers investigated drop collision and coalescence in linear flows ranging from simple shear flows to pure extensional flows generated by a four-roll mill. This mimics the range of conditions experienced by drops in real, complex applications. A review of their recent work was written by Leal (5).

Unlike experiments, numerical simulations have the potential advantage of being able to resolve the thin film between the drops. However, numerical investigations of binary drop collisions are rare. The study of Foote (6) emphasized bouncing of equal-sized water drops colliding head-on. The collision process was modeled using a Marker-and-Cell method as one drop colliding with a non-wetting slip wall. The effect of the surrounding air on drop motion was neglected. Mashayek et al. (7) employed a spine-flux method and focused their study on coalescing collisions of two drops colliding head-on under a fixed Weber number of 1. The effects of Reynolds number, internal circulation, and drop-size ratio on coalescence were examined. Nobari and Jan (8) investigated both bouncing and non-bouncing outcomes of head-on collisions of two equal-sized drops using a front-tracking method. The velocity and pressure field inside the bouncing drops were studied in detail. The effects of Reynolds number and Weber number were examined. However, in their study, coalescence did not occur naturally, but by artificially removing the thin film between the drops. The time when the film ruptured was found to affect the behavior of the combined drop. A three-dimensional version of the same method was used to simulate off-center binary collisions by Nobari and Tryggvason (9). Lafaurie et al. (10) presented sample three-dimensional computations of drop collision to illustrate their volume-of-fluid (VOF) method. Recently, Premnath and Abraham (11) simulated head-on and off-center drop collisions leading to coalescence and separation using axisymmetric and three-dimensional versions of the multiple-relaxation-time lattice-Boltzmann model, respectively. The effect of Weber number, Ohnesorge number, viscosity ratio, impact parameter, and the properties of the ambient fluid are examined. The full three-dimensional study of Pan and Suga (12) using a level-set method covers all major collision outcomes, except for fragmentation. The numerically determined regimes of bouncing, coalescence with major deformation, and separation were consistent with previous theoretical predictions.

However, they failed to predict the regime of coalescence with minor deformation, because they neglected intermolecular forces. For drop collisions in Stokes flows, the boundary-integral method is often used. Zinchenko et al. (13) presented a three-dimensional boundary-integral method to simulate the gravity-induced interaction of drops. The drops could come arbitrarily close to each other, but could not coalesce in their method. A simulation of collisions in shear and compressional flows can be found in the work of Cristini et al. (14). These authors have also conducted a theoretical study of head-on collisions of surfactant-covered drops (15).

When two equal-sized drops immersed in an immiscible fluid approach each other along the axis connecting their centers, a film forms between them and subsequently thins. When the thickness of the film falls into the range of several hundreds of Angstroms, 100–1000 Å, van der Waals forces become significant, leading to rupture of the film and consequently coalescence of the drops.

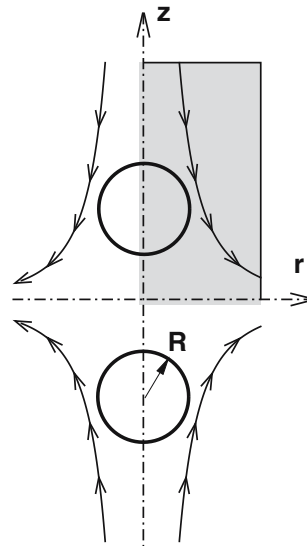
Although the literature in van-der-Waals-driven thin-film rupture is rich, most studies have focused on rupture of a free film [16, 17], or a thin film on a solid substrate (18). Studies on thinning and rupture of a thin film between drops, which is usually dimpled, in coalescence collisions are limited. Chen (19) included van der Waals forces in his model, describing the drainage and rupture of the dimpled thin film between two equal-sized drops. A number of assumptions were made in this study, including creeping flow and the lubrication approximation. The initial shape of the interface was determined in an ad hoc way. The evolution of the film shape was presented. Calculations at different strengths of van der Waals forces showed that the rupture time decreases with increasing strength of the van der Waals forces. Yiantsios and Davis (20) examined the effects of van der Waals forces on the rupture of the film between two different-sized drops as they approach each other due to gravity at small capillary and Reynolds numbers. The van der Waals forces were applied in the form of a negative disjoining pressure on the interface as a boundary condition. Lubrication theory was applied in the film. They found that large van der Waals forces lead to ‘nose rupture’ on the symmetry axis, and small van der Waals forces lead to off-center ‘rim rupture’. Chesters and co-workers have studied drainage and rupture of the liquid film between drops colliding at constant velocity (21), or under a constant interaction force (22) with the influence of van der Waals forces. Assumptions similar to those used in (20) were adopted.

In this study, we present the numerical simulation of the collision of two equal-sized drops driven by an extensional flow. In industrial applications, such as in mixers and nozzles, droplets may experience translation, shearing, and extension. Here we focus on extension as one of the key ingredients of real flows. The effects of van der Waals forces on the coalescence of the drops are examined. The van der Waals forces are calculated by two different methods. In one method, a body force acting on the drops and calculated from an interaction potential is introduced into the momentum equation (23). In the second method a disjoining pressure in the film is used to represent the van der Waals forces as in [17, 19]. The concept of disjoining pressure which accounts for the pressure difference between a thin film and the bulk phase from which the film is made was first introduced by Deryagin (24).

The primary difference between our research and previous work is that the Reynolds and capillary numbers need not be small, as in most of the other theoretical and computational studies. The full Navier–Stokes equations with modifications to represent van der Waals forces that govern the motion of the fluid both inside the drop and in the surrounding flow are solved. In addition, the whole coalescence process from the approach of the two drops, to the rupture of the film, to the formation of the single drop is examined. We start with two drops separated by a certain distance and the film between the drops develops naturally. Our goal is to develop a numerical model that can accurately simulate the collision of two drops and give us a better understanding of the dynamics.

Section 2 presents the problem studied, the governing equations, and the numerical methods. The two methods used to incorporate van der Waals forces are introduced in Sect. 3. Verification is presented in Sect. 4. Results and discussion are reported in Sect. 5. Section 6 is devoted to conclusions.

**Fig. 1** The physical problem and the computational domain (in gray). Two drops are propelled by a hyperbolic flow. The size of the computational domain is  $2.5 \times 5$  radii



## 2 Formulation

Two equal-sized spherical liquid drops are immersed in an axisymmetric extensional gas flow, as shown in Fig. 1. The drops are centered on the symmetry axis of the flow. Driven by the suspending fluid, the drops will collide head-on and then may bounce apart or come into contact.

An axisymmetric VOF method is used to simulate the collision of the two drops. The VOF method was first developed by Nichols et al. (25) and Hirt and Nichols (26). In this method, a volume fraction,  $F$ , is defined in each cell as the fraction of the volume of the cell containing liquid. Thus,  $F$  takes the value of one inside the liquid drops and zero inside the ambient gas. In cells containing both liquid and gas  $F$  takes other values. The interface is reconstructed based on the volume-fraction data. The motion of the interface is captured through the evolution of the volume fraction.

One set of equations that govern the motion in the whole domain is used. This includes both the drops and the ambient gas. The effort of applying boundary conditions on the interface is then saved, but the surface tension must be accounted for correctly. For this purpose, the continuum surface-force (CSF) method introduced by Brackbill et al. (27) is employed to calculate the surface tension. In this method, the volume fraction is smeared over a small region near the interface. The surface tension is treated as a volume force that varies continuously across the interface with nonzero values only in the smeared region near the interface. As the grid is refined and the thickness of this region goes to zero, the surface tension retrieves its exact value. For surface-tension coefficient  $\sigma$ , the volume force used to simulate surface tension can be expressed as  $\sigma\kappa\nabla F$ , where  $\kappa$  is the interface curvature.

For incompressible, transient, interfacial flows, the axisymmetric dimensionless governing equations are the continuity equation,

$$\frac{\partial u}{\partial r} + \frac{u}{r} + \frac{\partial v}{\partial z} = 0, \quad (1)$$

the Navier–Stokes equations,

$$\rho \left( \frac{\partial u}{\partial t} + u \frac{\partial u}{\partial r} + v \frac{\partial u}{\partial z} \right) = -\frac{\partial p}{\partial r} + \frac{1}{\text{Re}} \left[ 2 \frac{\partial}{\partial r} \left( \mu \frac{\partial u}{\partial r} \right) + \frac{\partial}{\partial z} \left( \mu \frac{\partial v}{\partial r} + \mu \frac{\partial u}{\partial z} \right) + 2\mu \frac{\partial}{\partial r} \left( \frac{u}{r} \right) \right] + \frac{\kappa}{\text{We}} \frac{\partial F}{\partial r} + f_{v,r}, \quad (2)$$

$$\rho \left( \frac{\partial v}{\partial t} + u \frac{\partial v}{\partial r} + v \frac{\partial v}{\partial z} \right) = -\frac{\partial p}{\partial z} + \frac{1}{\text{Re}} \left[ \frac{\partial}{\partial z} \left( \mu \frac{\partial v}{\partial z} \right) + \frac{\partial}{\partial r} \left( \mu \frac{\partial v}{\partial r} + \mu \frac{\partial u}{\partial z} \right) + \frac{\mu}{r} \left( \frac{\partial v}{\partial r} + \frac{\partial u}{\partial z} \right) \right] + \frac{\kappa}{\text{We}} \frac{\partial F}{\partial z} + f_{vz}, \tag{3}$$

and the volume-fraction convection equation,

$$\frac{\partial F}{\partial t} + u \frac{\partial F}{\partial r} + v \frac{\partial F}{\partial z} = 0, \tag{4}$$

where  $u$  is the velocity in the radial direction,  $v$  is the velocity in the vertical direction,  $\rho$  is the density,  $\mu$  is the viscosity,  $p$  is the pressure,  $\text{Re}$  is the Reynolds number,  $\text{We}$  is the Weber number, and  $f_{vr}$  and  $f_{vz}$  are the radial and vertical components of the van der Waals force  $\mathbf{f}_v$ . Gravity is neglected. The calculation of van der Waals forces will be introduced in the next section.

The length scale used in non-dimensionlization is the drop radius,  $R$ . The velocity scale is the strain rate of the hyperbolic flow,  $G$ , times  $R$ . Inertial time and pressure scales are used. These scalings are used in the rest of the paper except in Sect. 4.2.

The density and viscosity in Eqs. 2 and 3 are linear functions of the volume fraction

$$\rho = \hat{\rho} + (1 - \hat{\rho})F, \tag{5}$$

$$\mu = \hat{\mu} + (1 - \hat{\mu})F, \tag{6}$$

where  $\hat{\rho}$  is the density ratio,  $\hat{\rho} = \rho_g/\rho_d$ , and  $\hat{\mu}$  is the viscosity ratio,  $\hat{\mu} = \mu_g/\mu_d$ . The subscripts d and g denote the drop and the ambient gas, respectively.

The non-dimensional parameters are the Reynolds number,  $\text{Re} = \rho_d GR^2/\mu_d$ , the Weber number,  $\text{We} = \rho_d G^2 R^3/\sigma$ , the Hamaker number,  $A = \bar{A}/\rho_d R^5 G^2$ , where  $\bar{A}$  is the Hamaker constant, the density ratio, and the viscosity ratio.

The flow field is solved by a projection method [28, 29] on a staggered grid. The resulting pressure Poisson equation is solved using an incomplete Cholesky conjugate gradient method (30). The interface is reconstructed from the volume-fraction field at each time step using a piece-wise linear approximation. The volume fraction is convected by calculating the volume flux across each cell face. Coalescence is assumed to occur when any of the linear interface segments intersect the symmetry plane. The code, aside from the van der Waals forces, was thoroughly tested and used to study the breakup of a vibrating drop by James et al. (31, Chapter 6).

As shown in Fig. 1, the  $z$  axis is a symmetry axis and  $z = 0$  is a symmetry plane. To take advantage of symmetry, the first quadrant comprises the computational domain, shown as the shaded region in Fig. 1. The size of the computational domain is  $2.5 \times 5$ . Initially the two drops are placed on the axis of symmetry with their centers separated by four radii. The velocity of the flow field is initialized as  $u = r$  and  $v = -2z$ . This velocity is then maintained on the top and right boundaries. Symmetry conditions are imposed on the other boundaries. Boundary conditions for the pressure change between the current and next time step are derived from the velocity boundary conditions. The derivative of the pressure change normal to each boundary is zero.

The volume fraction is zero at the top and the right boundaries, and symmetric about the symmetry axis. Special attention is paid to the volume-fraction boundary condition on the symmetry plane. Since only one of the drops' profiles is tracked, the drop in the computational domain interacts with its mirror image through the volume-fraction boundary condition on the symmetry plane. Therefore the volume-fraction boundary condition plays a significant role in modeling the collision behavior. Two kinds of the volume-fraction boundary conditions are used:  $F = 0$  and  $\partial F/\partial z = 0$ , which lead to different collision outcomes. The results will be discussed in Sect. 5.2.

The volume-fraction boundary conditions are applied using the ghost cells outside the physical boundaries, as shown in Fig. 2. The volume fraction in each ghost cell is set to be zero if the zero boundary condition is used, and is equal to the volume fraction in the adjacent real cell if the symmetry boundary

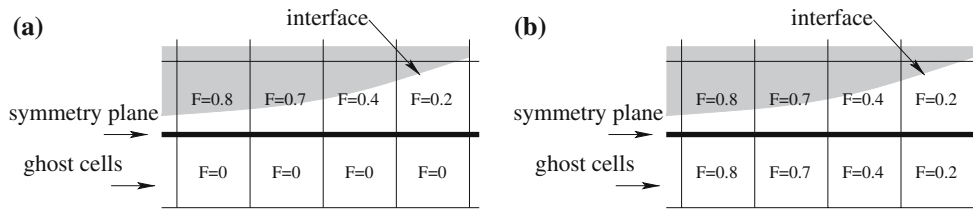


**Fig. 2** Illustration of the volume fraction boundary condition on the symmetry plane. **(a)** zero condition, **(b)** symmetry condition

condition is used. If the volume fraction in the ghost cells is zero, the drop in the computational domain can not ‘see’ the mirror drop. It can only ‘see’ the boundary as a non-wetting slip wall. However, symmetry conditions for the velocity and pressure mimic collision. Consequently, the drop can not merge with the mirror drop and will bounce. In general, in the VOF method, two interfaces will merge automatically whenever they move into adjacent cells. If the symmetry boundary condition is used, this leads to coalescence of the drops. Unfortunately, the volume-fraction information of the mirror drop will corrupt the reconstruction of the simulated drop as well as the computation of curvature and in turn the surface tension. In our simulations, the symmetry and zero conditions enable us to simulate not only coalescence, but also bouncing. However, resolution of the two separate, but nearby, interfaces in the coalescing case is somewhat problematic. Future work will address this issue.

### 3 Calculation of van der Waals forces

We have developed two different methods to calculate van der Waals forces. One method represents van der Waals forces directly as the interaction force between the drops. The other method accounts for the van der Waals forces via a disjoining pressure in the film between the drops.

In the first method, the interaction potential between the two drops due to van der Waals forces is computed first. Then the body force acting on the drop is the negative gradient of the van der Waals potential. The body force, which is attractive since the two drops are of the same material (32, Chapter 12), is then introduced into the momentum equation. Since the flow in the whole domain is computed simultaneously, the body force exerts its influence on the thinning and rupture of the film between the drops via the interface.

Numerically the van der Waals forces  $\mathbf{f}_v$  are calculated as follows. The potential energy between the two drops is calculated via a microscopic Hamaker procedure [23, 33]. The interactions with gas molecules are neglected.

The potential energy of a molecule located in the cylindrical cell  $(m, n)$  in the simulated drop  $i$  due to a molecule in the cell  $(s, t)$  in the mirror drop  $j$  is

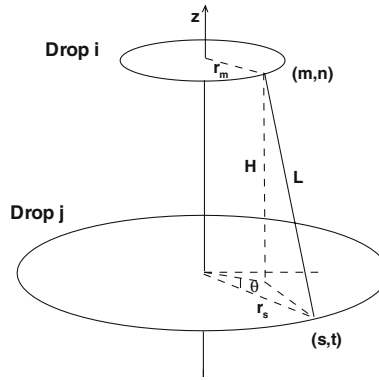
$$-\lambda_{ij}/L^6, \tag{7}$$

where  $\lambda_{ij}$  is the dimensionless London constant, which is related to the London constant  $\bar{\lambda}_{ij}$  as  $\lambda_{ij} = \bar{\lambda}_{ij}/\rho_d R^{11} G^2$ , and  $L$  is the distance between the two molecules, as shown in Fig. 3. For small grid spacings, the two molecules are approximately at the centers of the two cells whose coordinates are  $(r_m, z_m)$  and  $(r_s, z_s)$ .  $L$  then becomes

$$L = \sqrt{H^2 + (r_m^2 + r_s^2 - 2r_m r_s \cos \theta)}, \tag{8}$$

where  $H = z_n - z_t$  is the vertical distance between the two molecules, and  $\theta$  is shown in Fig. 3.

**Fig. 3** A molecule in cell  $(m, n)$  in the simulated drop  $i$  interacts with a molecule in cell  $(s, t)$  in the mirror drop  $j$



The potential energy of a molecule in cell  $(m, n)$  due to all the molecules in cell  $(s, t)$  is obtained by multiplying Eq. 7 by the volume fraction in  $(s, t)$ ,  $F_{st}$ , and the number of molecules per unit volume in drop  $j$ ,  $N_j$ , and integrating over the cell volume,

$$d\phi_{mn} = \int_{\text{cell}(s,t)} -\frac{\lambda_{ij}}{L^6} N_j F_{st} r dr d\theta dz, \tag{9}$$

where  $N_j$  is related to its dimensional form  $\bar{N}_j$  as  $N_j = R^3 \bar{N}_j$ . Eq. 9 is approximated as

$$d\phi_{mn} \simeq -\lambda_{ij} N_j r_s \Delta r \Delta z F_{st} \int_0^{2\pi} \frac{1}{L^6} d\theta \tag{10}$$

for small grid spacings in the  $r$  and  $z$  directions,  $\Delta r$  and  $\Delta z$ , respectively. The integral  $\int_0^{2\pi} 1/L^6 d\theta$  is evaluated as

$$\int_0^{2\pi} \frac{d\theta}{L^6} = 2\pi \left\{ \frac{(H^2 + r_s^2 + r_m^2)^2 + 2r_s^2 r_m^2}{[(H^2 + r_s^2 + r_m^2)^2 - (2r_s r_m)^2]^{5/2}} \right\}. \tag{11}$$

Thus,

$$d\phi_{mn} = -2\pi \lambda_{ij} N_j r_s \Delta r \Delta z F_{st} \left\{ \frac{(H^2 + r_s^2 + r_m^2)^2 + 2r_s^2 r_m^2}{[(H^2 + r_s^2 + r_m^2)^2 - (2r_s r_m)^2]^{5/2}} \right\}. \tag{12}$$

The potential energy per unit volume in cell  $(m, n)$  due to the entire drop  $j$  is computed by summing over all cells in drop  $j$ ,

$$\begin{aligned} \phi_{mn} &= -2\pi \lambda_{ij} N_i N_j \Delta r \Delta z \times \sum_{s,t} \left\{ r_s F_{st} \frac{(H^2 + r_s^2 + r_m^2)^2 + 2r_s^2 r_m^2}{[(H^2 + r_s^2 + r_m^2)^2 - (2r_s r_m)^2]^{5/2}} \right\} \\ &= -\frac{2A}{\pi} \Delta r \Delta z \sum_{s,t} \left\{ r_s F_{st} \times \frac{(H^2 + r_s^2 + r_m^2)^2 + 2r_s^2 r_m^2}{[(H^2 + r_s^2 + r_m^2)^2 - (2r_s r_m)^2]^{5/2}} \right\}, \end{aligned} \tag{13}$$

where  $N_i$  is the number of molecules per unit volume in drop  $i$ , which is related to its dimensional form  $\bar{N}_i$  as  $N_i = R^3 \bar{N}_i$ . Note that the Hamaker constant,  $\bar{A} = \pi^2 \bar{N}_i \bar{N}_j \lambda_{ij}$ .

The force per unit volume at  $(m, n)$  is

$$\mathbf{f}_v = -F_{mn} \nabla \phi_{mn}, \tag{14}$$

where  $\phi$  is computed from Eq. 13 and central differencing is used to evaluate Eq. 14. This force is weighted by the volume fraction,  $F_{mn}$ , to ensure that the force is applied only inside the drop.

In the second method, the effect of van der Waals forces is incorporated as a disjoining pressure in the film between the drops. According to Deryagin (24), the disjoining pressure can be introduced into the equation of motion. For a plane-parallel film with thickness  $h$ , the disjoining pressure is given by [20, 23, 33]

$$\Pi(h) = -\frac{A}{6\pi h^3}. \tag{15}$$

The gap between the two drops is not uniform, especially when the distance between the drops is large, but we assume that the van der Waals forces are negligible when the drops are far away. When the drops are close enough for the van der Waals forces to be important, we assume that the slope of the interface is small. It is then appropriate to use Eq. 15 to approximate the disjoining pressure in the film. The validity of these assumptions will be examined in Sect. 5.3.

The van der Waals force reads

$$\mathbf{f}_v = -\nabla \left( \frac{A}{6\pi h^3} \right). \quad (16)$$

Since the disjoining pressure depends only on the thickness of the film only,

$$\frac{\partial}{\partial z} \left( \frac{A}{6\pi h^3} \right) = 0. \quad (17)$$

The van der Waals force is then

$$\mathbf{f}_v = -\frac{\partial}{\partial r} \left( \frac{A}{6\pi h^3} \right) \hat{r}, \quad (18)$$

which is evaluated using second-order central differencing. In the computation, the film thickness  $h$  is defined only inside the film between the drops. It is calculated as the average height of the liquid in a cell column.

## 4 Validation

In this section the two methods to calculate van der Waals forces are validated. Then the effect of grid resolution on coalescence time is studied. We have also studied the effect of domain size. The results show that the computational domain used is sufficient to capture the collision dynamics for the parameters used. The details are not presented here.

### 4.1 Validation of the potential method

The interaction potential and force between two spheres separated by a distance  $\mathcal{H}$  are known (33). The potential  $\Phi$  for two equal-sized drops is

$$\Phi = -\frac{A}{12} \left[ \frac{1}{x^2 + 2x} + \frac{1}{x^2 + 2x + 1} + 2 \log \frac{x^2 + 2x}{x^2 + 2x + 1} \right], \quad (19)$$

and the interaction force  $\mathcal{F}$  is

$$\mathcal{F} = -\frac{A(x+1)}{12} \left[ \frac{1}{(x^2 + 2x)^2} + \frac{1}{(x^2 + 2x + 1)^2} - \frac{2}{x^2 + 2x} + \frac{2}{x^2 + 2x + 1} \right], \quad (20)$$

where  $x = \mathcal{H}/2$ .

Consider the two spheres in Fig. 1 which are separated by a distance  $\mathcal{H} = 2R$ . The interaction potential and force in each grid cell are computed numerically and the totals are obtained by summing the values in all the cells. The results are compared with the exact values obtained from Eqs. 19 to 20. The relative error is summarized in Table 1. It can be seen that the error is very small and has a convergence rate of about 2.

### 4.2 Validation of the disjoining pressure method

To verify the disjoining pressure method for calculating van der Waals forces, we simulate the van-der-Waals-driven axisymmetric point rupture of a free film and compare with previous results [16, 17]. Ida and

**Table 1** Relative error in the computation of interaction potential and force between two equal-sized drops separated by a distance of  $2R$

| Number of grid cells | Error in potential (%) | Rate | Error in force (%)    | Rate |
|----------------------|------------------------|------|-----------------------|------|
| $50 \times 100$      | $6.94 \times 10^{-2}$  |      | $7.30 \times 10^{-2}$ |      |
| $71 \times 142$      | $3.41 \times 10^{-2}$  | 2.03 | $4.30 \times 10^{-2}$ | 1.51 |
| $100 \times 200$     | $1.72 \times 10^{-2}$  | 2.00 | $2.31 \times 10^{-2}$ | 1.81 |
| $142 \times 284$     | $8.14 \times 10^{-3}$  | 2.13 | $1.02 \times 10^{-2}$ | 2.33 |
| $200 \times 400$     | $4.29 \times 10^{-3}$  | 1.87 | $4.68 \times 10^{-3}$ | 2.27 |

Miksis (16) studied the line rupture of a two-dimensional free film using a long-wavelength model, as did Vaynblat et al. (17). Vaynblat et al. also examined point rupture and found similar behavior to that of line rupture. Vaynblat et al. have confirmed numerically that for both line and point rupture, near the rupture time  $t_c$  and the rupture point  $r_c$ , the solutions to the long-wavelength lubrication equations (17) describing rupture have similarity forms

$$h(r, t) = \tau^\alpha H(\eta), \tag{21}$$

$$u(r, t) = \tau^\gamma U(\eta), \tag{22}$$

where  $\tau = t - t_c$ ,  $\eta = (r - r_c)/\tau^\beta$ ,  $h$  is the film thickness, and the constants  $\alpha$ ,  $\beta$ , and  $\gamma$  are scaling exponents. Dimensional analysis based on the continuity equation gives

$$\gamma - \beta = -1. \tag{23}$$

The two studies disagree about the dynamic balance between different terms, and thus the scaling exponents values. Ida and Miksis suggested a balance between van der Waals forces and viscosity while neglecting inertia and surface tension, leading to  $\alpha = 1/3$  while  $\beta$  and  $\gamma$  were undetermined by scaling. The values of  $\beta$  inferred from their numerical simulations are  $0.39 \sim 0.46$  (17). In contrast, Vaynblat et al. argued that the balance is between van der Waals forces, viscosity and inertia while surface tension neglected. This scaling results in the determination of all the three scaling exponents

$$\alpha = 1/3, \quad \beta = 1/2, \quad \gamma = -1/2. \tag{24}$$

Using a highly adaptive mesh, Vaynblat et al. solved the lubrication equations numerically and were able to resolve the dynamics until a time very close to rupture when the film thickness is of order  $10^{-10}$  as opposed to  $10^{-3}$  in (16). The values for the scaling exponents in Eq. 24 were verified.

We adopt the problem studied in both (16) and (17), but solve the full Navier–Stokes equations in an axisymmetric coordinate system. It is difficult to implement the potential method to compute the van der Waals forces because the film extent is infinite and the coordinate system is axisymmetric. Therefore, only the disjoining pressure method is used.

The characteristic scales are: length  $h_0$ , velocity  $\mu/\rho h_0$ , time  $\rho h_0^2/\mu$ , and pressure  $\mu^2/\rho h_0^2$ , where  $h_0$  is the mean thickness of the film,  $\rho$  is the density of the film, and  $\mu$  is the viscosity of the film. To compare with the results in (17), the dimensionless parameter values in our scaling are

$$\text{Re} = 1, \quad \text{We} = \pi^2/3, \quad \text{and} \quad A = 6\pi\epsilon^2, \tag{25}$$

where  $\epsilon$  is the ratio of the mean thickness of the film to the radial extent of the domain. The effect of varying the parameter  $\epsilon$  will be considered. Since the film in (17) is in a vacuum, a small value is chosen for the density and viscosity ratios:  $\hat{\rho} = \hat{\mu} = 0.01$ . Additional simulations showed that this value is sufficiently small to have no effect on the results.

To take advantage of symmetry, only a quarter of the film profile is used as the computation domain which is taken to be  $[0, 1/\epsilon] \times [0, 1]$ . The symmetry volume-fraction boundary condition is used on the symmetry plane. The initial film profile is the same as in (17). The half film thickness is  $0.5h(r, 0) = 0.5 - 0.1 \cos(\epsilon\pi r)$ .

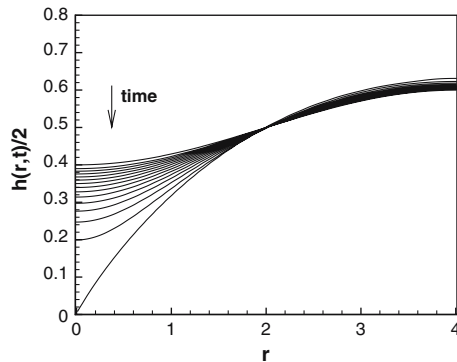


**Fig. 4** Time evolution of an unstable thin film. A series of the film half-thickness is shown for  $t = 0$  to  $t = 26$  in increment of 2 units, and a final profile at  $t = 27.70$  at the time of rupture.  $\epsilon = 1/4$ ,  $\text{Re} = 1$ ,  $\text{We} = \pi^2/3$ ,  $A = 3\pi/8$ ,  $\Delta r = \Delta z = 0.02$

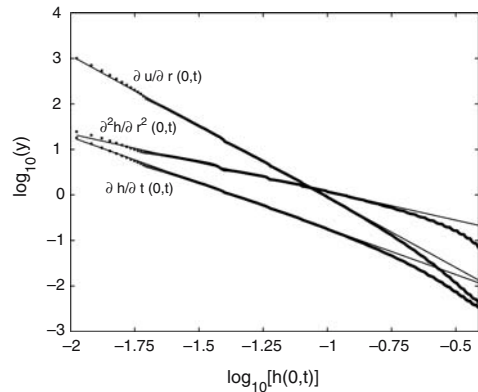


**Fig. 5** Log-log plots of  $-\partial h/\partial t(0,t)$ ,  $\partial^2 h/\partial r^2(0,t)$ , and  $\partial u/\partial r(0,t)$  for the case shown in Fig. 4.  $\epsilon = 1/4$ ,  $\text{Re} = 1$ ,  $\text{We} = \pi^2/3$ ,  $A = 3\pi/8$ ,  $\Delta r = \Delta z = 0.02$ . Symbols are numerical data and solid lines are linear fits

The calculation in (17) is one dimensional, so only the velocity in the  $r$  direction is defined and initially is  $u = 0.1\epsilon \sin(\epsilon\pi r)$ . In our simulation, this initial condition for  $u$  is used in the film. The initial  $u$  in the gas is obtained from mass conservation. The initial  $v$  velocity in the film and in the gas are derived from the continuity equation. Since the similarity solution is independent of the initial conditions, we should obtain the same similarity solution even though we use a slightly different initial condition. Other forms of initial conditions have also been tested; the results show that while different initial conditions affect the rupture time, they have little effect on the similarity solution.

As a representative example, Fig. 4 shows the time evolution of the film for  $\epsilon = 1/4$ . The scaling exponents can be estimated from log-log plots of appropriate variables as in (17). The slope of  $-\partial h/\partial t(0,t)$  versus the minimum film thickness  $h(0,t)$  on a log-log scale is  $(\alpha - 1)/\alpha$ . Similarly  $\partial^2 h/\partial r^2(0,t)$  gives  $(\alpha - 2\beta)/\alpha$ , and  $\partial u/\partial r(0,t)$  gives  $(\gamma - \beta)/\alpha$ . Figure 5 shows the log-log plots of the above variables as functions of  $h(0,t)$  for  $\epsilon = 1/4$ . All variables approach linear behavior in the late stages of the thinning of the film, which implies the existence of the similarity solution.

A systematic study has been conducted for different values of  $\epsilon$  and different grid resolutions. In (16) and (17),  $\epsilon \ll 1$  is the basic assumption for the lubrication model. However, since the full Navier–Stokes equations are solved in our simulation, computational cost prevents us from using very small  $\epsilon$  as well as very fine grids which are important for resolving the thin film near rupture. Despite of these limitations, by varying  $\epsilon$  and the resolution we can show that our results approach those in (16) as  $\epsilon$  decreases or as the resolution is refined.

The computed slopes and the exponents estimated from these slopes are summarized in Tables 2 and 3. The results of previous studies (16,17) are also listed. The slopes of  $-\partial h/\partial t$  and  $\partial u/\partial r$  have a reasonable agreement with the theoretical values. Therefore, the constant  $\alpha$  and the relationship in Eq. 23 are reproduced. The slope of  $-\partial h/\partial t$  deviates from its theoretical value with decrease of  $\epsilon$ , whereas it converges with increase of resolution. This implies that for small  $\epsilon$  a finer grid is needed.

Although the slope of  $\partial^2 h/\partial r^2$  converges as  $\epsilon$  decreases and as the resolution is refined, the current values differ from the theoretical ones, but are consistent with the work of Ida and Miksis (16). The main reason for this discrepancy is resolution. As discussed by Vaynblat et al. (17), when surface tension is small compared with viscosity, as in the current case, a transition region, in which inertial effects are subdominant, exists before van der Waals forces, viscosity and inertia all balance. Vaynblat et al. also pointed out that the values of  $\beta$  estimated from the results of Ida and Miksis did not fall into the range required by their scaling. Furthermore, Vaynblat et al. were able to resolve the film up to  $10^{-10}$  compared to  $10^{-3}$

**Table 2** Computed slopes and estimated exponents as a function of  $\epsilon \Delta r = \Delta z = 0.02$

| $\epsilon$           | Slopes  |  |   | Exponents |                  |         |
|----------------------|---|--|---|-----------|------------------|---------|
|                      | $-\frac{\partial h}{\partial t}$<br>$(\alpha - 1)/\alpha$ | $\frac{\partial u}{\partial r}$<br>$(\gamma - \beta)/\alpha$ | $\frac{\partial^2 h}{\partial r^2}$<br>$(\alpha - 2\beta)/\alpha$ | $\alpha$  | $\gamma - \beta$ | $\beta$ |
| 1/3                  | -1.9986   | -3.1092  | -1.2233   | 0.3335    | -1.0369          | 0.3707  |
| 1/4                  | -2.0183   | -3.1080  | -1.2660   | 0.3313    | -1.0297          | 0.3754  |
| 1/5                  | -2.0312   | -3.1066  | -1.2941   | 0.3299    | -1.0249          | 0.3784  |
| Ida and Miksis (16)  |   |  |   | 0.3359    | -1.0143          | 0.3904  |
| Vaynblat et al. (17) | -1.9999   | -2.9999  | -2.000  | 0.3333    | -1.0000          | 0.5000  |
| Theory (17)          | -2  | -3   | -2  | 1/3       | -1               | 1/2     |

**Table 3** Computed slopes and estimated exponents as a function of grid resolution  $\epsilon = 1/5$

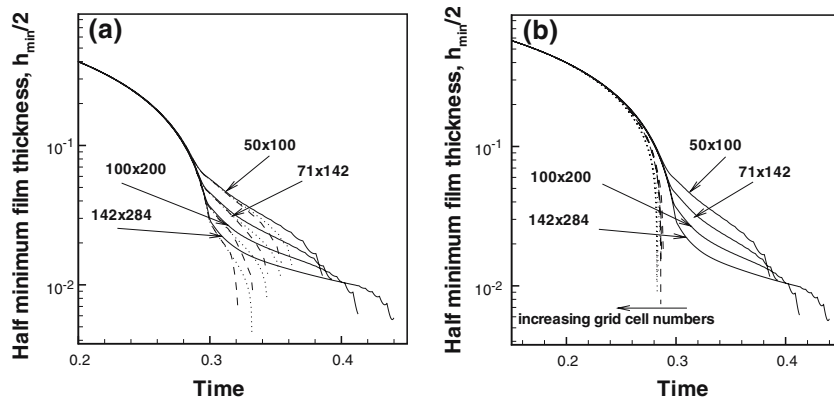
| $\Delta r = \Delta z$ | Slopes  |  |   | Exponents |                  |         |
|-----------------------|---|--|---|-----------|------------------|---------|
|                       | $-\frac{\partial h}{\partial t}$<br>$(\alpha - 1)/\alpha$ | $\frac{\partial u}{\partial r}$<br>$(\gamma - \beta)/\alpha$ | $\frac{\partial^2 h}{\partial r^2}$<br>$(\gamma - 2\beta)/\alpha$ | $\alpha$  | $\gamma - \beta$ | $\beta$ |
| 1/30                  | -2.0812   | -3.2149  | -1.2558   | 0.3245    | -1.0432          | 0.3660  |
| 1/40                  | -2.0608   | -3.1651  | -1.2672   | 0.3267    | -1.0340          | 0.3703  |
| 1/50                  | -2.0312   | -3.1066  | -1.2941   | 0.3299    | -1.0249          | 0.3784  |
| Ida and Miksis (16)   |   |  |   | 0.3359    | -1.0143          | 0.3904  |
| Vaynblat et al. (17)  | -1.9999   | -2.9999  | -2.000  | 0.3333    | -1.0000          | 0.5000  |
| Theory (17)           | -2  | -3   | -2  | 1/3       | -1               | 1/2     |

in Ida and Miksis’s study, which enabled Vaynblat et al. to confirm that the balance at the final rupture stage is between van der Waals forces, viscosity and inertia. Vaynblat et al. also observed that  $\frac{\partial^2 h}{\partial r^2}$  took a longer time to approach linear behavior than other variables, which showed the existence of the transition region. Therefore, Vaynblat et al. concluded that the simulation of Ida and Miksis was still in the transient region. Due to computational intensity, the smallest film thickness we can resolve is about  $10^{-2}$ . Our calculated value of  $\beta$  is  $0.37 \sim 0.38$ , which is close to the value of 0.39 in the results of Ida and Miksis for the specific case considered. Considering the observation of Vaynblat et al., we conclude that our calculation has not reached the eventual rupture region, hence the values of  $\beta$  and  $\gamma$  observed disagree with the theoretical values in Eq. 24.

### 4.3 Effect of grid resolution

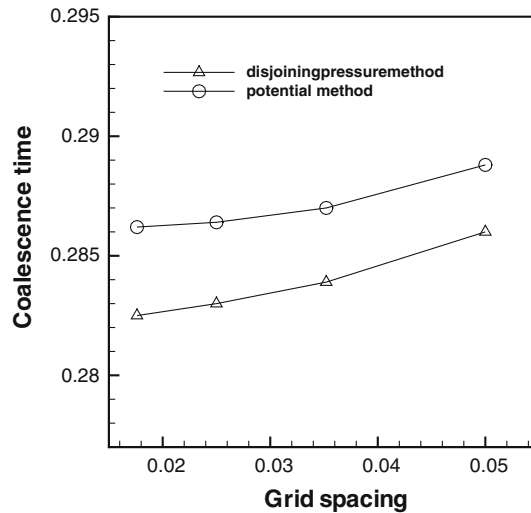
It has been shown (20) that the film between two deformable drops can not rupture in finite time in the absence of van der Waals forces. However, as mentioned in Sect. 2, in the VOF method, coalescence occurs automatically whenever two interfaces come into adjacent grid cells, whether the van der Waals forces are present or not. Therefore, it is of interest to investigate the effect of grid resolution on coalescence.

Figure 6 shows the time evolution of the half minimum film thickness  $h_{\min}/2$  for different numbers of grid cells and for rim rupture and nose rupture. The curves of different resolution overlap at small times, indicating that all the grids used are adequate to capture the large-scale motion of the drops. However, the film draining process is quite different. In the absence of the van der Waals forces, as the cell size decreases, the film ruptures at smaller thickness and thus the rupture time increases. On the contrary, in the presence of the van der Waals forces, the rupture time decreases with decreasing cell size. This reveals that as the film is better resolved, the van der Waals forces are better approximated so that their effects are more obvious. It can also be seen from figure (a) that the thinning rate of the film after a dimple forms increases



**Fig. 6** Half minimum thickness  $h_{\min}/2$  as a function of time for different grid resolution.  $\partial F/\partial z = 0$  boundary condition on the symmetry plane.  $Re = 1$ ,  $We = 1$ ,  $\hat{\rho} = 0.001$ ,  $\hat{\mu} = 0.001$ . Solid lines: van der Waals forces are absent; Dashed lines: van der Waals forces calculated from potential; Dotted lines: van der Waals forces calculated from disjoining pressure. **(a)**  $A = 0.1$ , **(b)**  $A = 10$

**Fig. 7** Coalescence time for the cases with van der Waals forces in Fig. 6(b)



as the grid is refined. Taking Figs. 13–15 together, one can see that this means the size of the dimple is decreasing. Thus the rupture mode is approaching nose rupture as the resolution increases, which implies that the Hamaker number used is relatively large. However, it is expected that smaller, more realistic, Hamaker numbers can be employed while using a very fine grid. The coalescence times for figure (b) in the presence of van der Waals forces are shown in Fig. 7. The coalescence time is converging with grid resolution.

### 5 Results and discussion

In this section the results of drop collision in the absence of the van der Waals forces are presented first. The significance of the volume fraction boundary condition on the symmetry plane is discussed. Then the effects of van der Waals forces, Reynolds number, and viscosity ratio are examined.

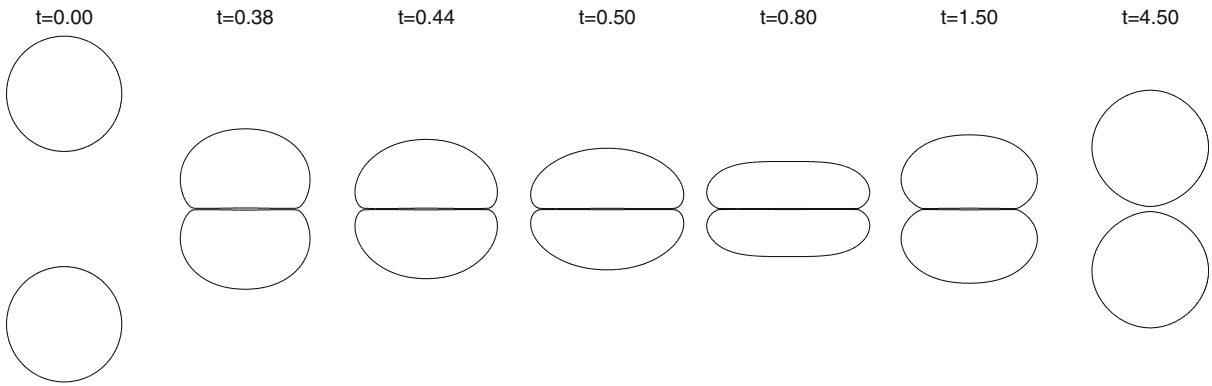


**Fig. 8** Rebound of the two drops. Van der Waals forces are absent.  $F = 0$  boundary condition on the symmetry plane.  $Re = 1$ ,  $We = 1$ ,  $\hat{\rho} = 0.001$ ,  $\hat{\mu} = 0.001$ ,  $142 \times 284$  grid cells

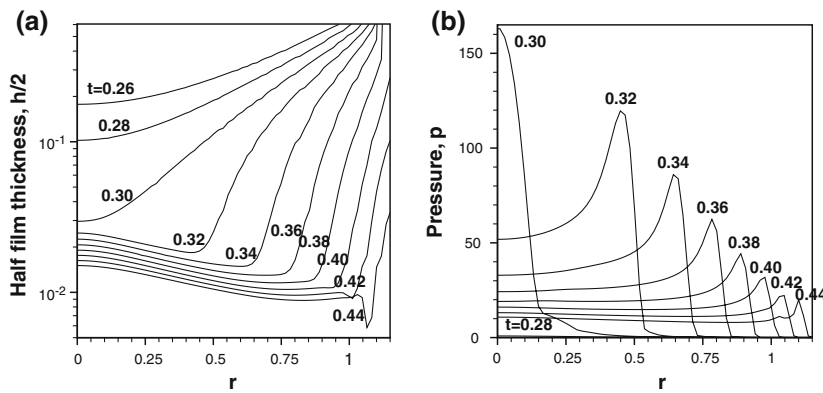


**Fig. 9** (a) Evolution of the film between the two drops. (b) Symmetry plane pressure as a function of time and radial position. Van der Waals forces are absent.  $F = 0$  boundary condition on the symmetry plane.  $Re = 1$ ,  $We = 1$ ,  $\hat{\rho} = 0.001$ ,  $\hat{\mu} = 0.001$ ,  $142 \times 284$  grid cells

### 5.1 Drop bouncing

In this and the next two sections,  $\hat{\rho}$  and  $\hat{\mu}$  are both specified as 0.001.  $Re = 1$ ,  $We = 1$  are used so that the effects of inertia, viscosity and surface tension are of equal importance.

As discussed in Sect. 2, unlike the other variables, the volume fraction has selective boundary conditions on the symmetry plane. Different boundary conditions are used to model different collision behaviors. Figure 8 shows the rebound of the two drops. Note the computational domain, comprised of  $142 \times 284$  grid cells, encompasses the first quadrant only, but its mirror images are shown for clarity. The straight-line approximation in each interfacial grid cell is plotted, which is necessary to represent the interface correctly near the symmetry plane. The zero volume-fraction boundary condition on the symmetry plane is used. Therefore the drop experiences the boundary as a slip wall, and cannot merge with its image. It is well known [19, 20] that as two drops approach each other the pressure between them builds up, leading to the formation of a dimple, as shown in the  $t = 0.38$  frame. Due to the large pressure build up, the drops rebound even though the applied hyperbolic flow continues to force them toward each other.

Figure 9(a) provides detailed shapes of the film between the drops. Unlike the coalescence case, the dimpled film does not rupture, but flattens as the drops deform. As the drops rebound, the film resumes its dimpled shape until the drops are almost round. Figure 9(b) shows the pressure at the symmetry plane as a function of time and radial position.

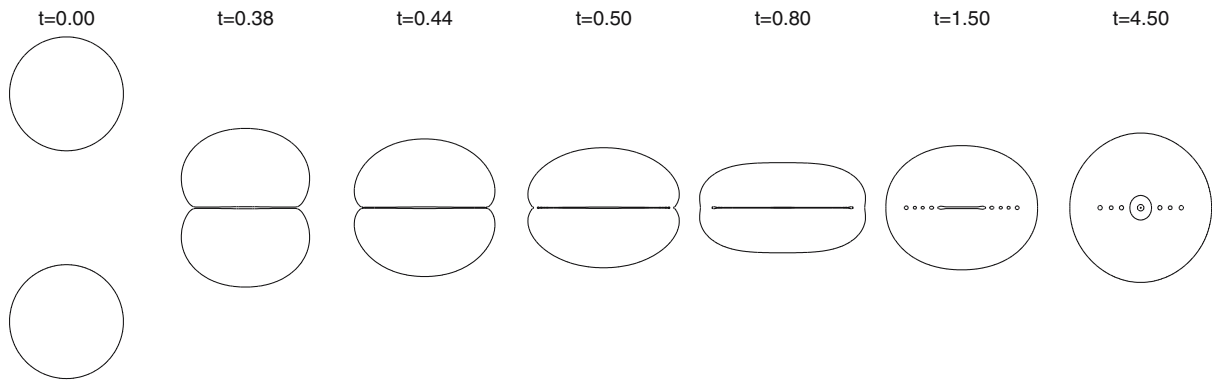


**Fig. 10** Coalescence of two drops. Van der Waals forces are absent.  $\partial F/\partial z = 0$  boundary condition on the symmetry plane.  $Re = 1$ ,  $We = 1$ ,  $\hat{\rho} = 0.001$ ,  $\hat{\mu} = 0.001$ ,  $142 \times 284$  grid cells

## 5.2 Drop coalescence

Figure 10 provides a general picture of the coalescence collision. In this case, the symmetry boundary condition is used. As a result, the drop and its image merge automatically. A dimple forms at  $t = 0.38$ . At  $t = 0.44$ , coalescence occurs at the rim of the dimple, resulting in high curvature at the contact point and subsequently a large surface tension force there. The contact area is then increased by surface tension, leaving a bubble trapped in the center. After the post-collision drop has reached its maximum deformation at  $t = 0.80$ , it and the entrapped bubble relax to a rounder shape.

In Fig. 10 the gross motion of the two drops is captured, but some of the details are not physical due to the limitation of axisymmetry. For instance, experimentally it is seen that azimuthal instabilities lead to coalescence at a point (34), not along the entire ring that surrounds the dimple. However, azimuthal variations are not allowed in this simulation. This limitation also allows the formation of toroidal bubbles in the simulation, which is certainly non-physical.

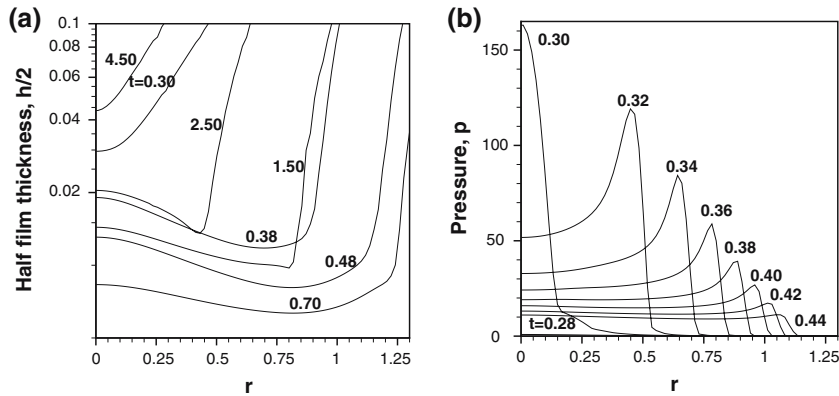
Details of the evolution of the film between the drops before coalescence are shown in Fig. 11(a). This figure shows the half thickness of the film between the drops,  $h/2$ , as a function of time and radial position. The interface translates downward with little deformation until  $t = 0.30$  when the interface near the symmetry axis flattens. After that a dimple forms and grows rapidly, the minimum thickness of the film decreases, and the film ruptures at the rim of the dimple at  $t = 0.44$ .

Figure 11(b) shows the pressure at the symmetry plane as a function of time and radial position. It is quite similar to Fig. 9(b) for the bouncing case. It illustrates the pressure evolution in the film between the drops. From  $t = 0.28$  to  $t = 0.30$ , there is a dramatic increase in pressure at the symmetry axis. The pressure peak then moves radially outward with the dimple. The thinning rate at the symmetry axis slows down under such a sudden increase of pressure, as shown in Fig. 12. The film at the symmetry axis thins quickly until a transition point at about  $t = 0.30$  and then thins slowly until just before the time of rupture. The curves of half film thickness at the symmetry axis  $h_c/2$  and half minimum thickness  $h_{\min}/2$  deviate at around the same time, indicating the formation of the dimple.

As shown by the above results, by manipulating the volume fraction boundary condition on the symmetry plane, we can simulate both coalescence and bouncing. However, the current model can not predict whether these two drops should merge or bounce. This will be the subject of future work.

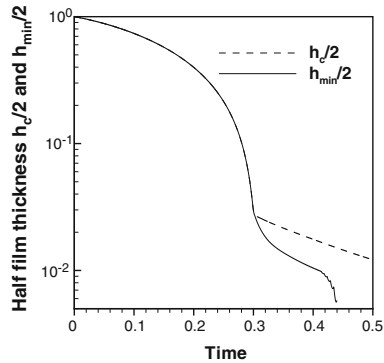
## 5.3 Effect of the van der Waals forces

When the film between the drops is sufficiently thin, van der Waals forces become significant and destabilize the film. In this section we focus on the effects van der Waals forces have on the rupture of the film. For this reason, the symmetry volume fraction boundary condition is used on the symmetry plane and van der



**Fig. 11** (a) Evolution of the film between the two drops. (b) Symmetry plane pressure as a function of time and radial position. Van der Waals forces are absent.  $\partial F/\partial z = 0$  boundary condition on the symmetry plane.  $Re = 1$ ,  $We = 1$ ,  $\hat{\rho} = 0.001$ ,  $\hat{\mu} = 0.001$ ,  $142 \times 284$  grid cells

**Fig. 12** Half film thickness at the symmetry line  $h_c/2$  and half minimum thickness  $h_{min}/2$  as a function of time. Van der Waals forces are absent.  $\partial F/\partial z = 0$  boundary condition on the symmetry plane.  $Re = 1$ ,  $We = 1$ ,  $\hat{\rho} = 0.001$ ,  $\hat{\mu} = 0.001$ ,  $142 \times 284$  cells



Waals forces are turned off once coalescence occurs. The dimensionless Hamaker number,  $A$ , is varied to adjust the strength of van der Waals forces. Four different values, which correspond to increasing strength of van der Waals forces, are used:  $A = 0.01$ ,  $A = 0.1$ ,  $A = 1$ , and  $A = 10$ .

5.3.1 Van der Waals forces calculated from potential

Figure 13 shows the evolution of the film between the drops for four values of  $A$ . Two modes of rupture are observed for different values of  $A$ : ‘rim rupture’ (20) where the film ruptures at the rim of the dimple, as in Fig. 13(a–c); and ‘nose rupture’ (20) where the film ruptures at the symmetry axis, as in Fig. 13(d). These two modes of rupture were also observed and discussed by Yiantsios and Davis (20) and Rother et al. (35). At relatively small  $A$ , for example  $A = 0.01$ , a dimple is formed and grows. However, the size of the dimple is smaller than the dimple in Fig. 11(a) in which  $A = 0$ . The size of the dimple continues to decrease as  $A$  increases. At  $A = 1$  only a very small dimple is formed. As  $A$  is increased to 10, no dimple is formed at all. The rupture mode changes from rim rupture to nose rupture. This suggests that under strong van der Waals forces, the drops approach each other so quickly that there is no time for a dimple to form.

Another fact apparent in Fig. 13 is that the rupture time decreases as the strength of the van der Waals forces grows. This point is also illustrated in Fig. 14(a) where the half minimum thickness of the film is shown as a function of time for different values of  $A$ . For small time, all the curves collapse with the curve  $A = 0$ , which implies that in this period of time van der Waals forces are weak. Thus the assumption that the van der Waals forces are negligible at large separation of the drops, which is used when introducing the disjoining method, is valid. As  $A$  increases, the film thins faster, therefore the corresponding curve

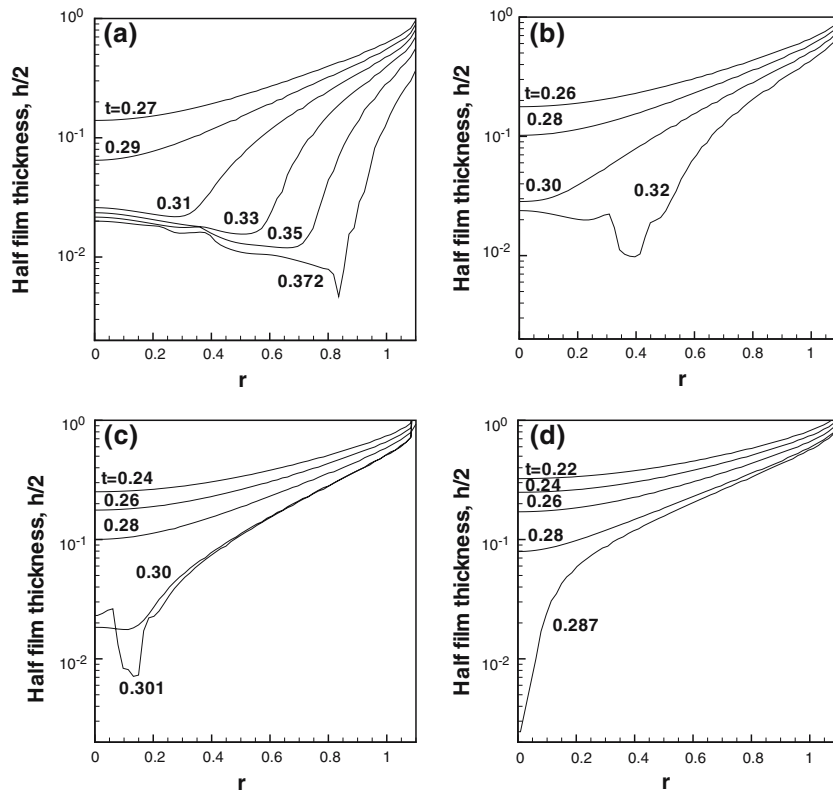


**Fig. 13** Evolution of the film between the drops with van der Waals forces calculated from potential.  $Re = 1$ ,  $We = 1$ ,  $\hat{\rho} = 0.001$ ,  $\hat{\mu} = 0.001$ ,  $142 \times 284$  grid cells. **(a)**  $A = 0.01$ , **(b)**  $A = 0.1$ , **(c)**  $A = 1$ , **(d)**  $A = 10$

deviates from the  $A = 0$  curve sooner. In addition, it can be seen that at small  $A$ , the curves with van der Waals forces deviate around the time when the dimple is formed. This implies that the van der Waals forces become important at that time. The  $A = 10$  curve deviates sooner, before dimple formation, showing that van der Waals forces become important earlier. Figure 13 shows that in the cases with a dimple the slope of the film is small after the dimple forms (this is more apparent if the figure is not plotted in the semi-log scale). This fact validates the second assumption in the disjoining pressure method.

It is also interesting to note the change of the thinning rate of the film under different values of  $A$ . As mentioned in Sect. 5.2, a transition point which is associated with the formation of the dimple exists, separating the faster thinning in early time and the slower thinning in later time, as shown on the curve  $A = 0$ . One expects that under stronger van der Waals forces the film will thin faster. At  $A = 0.01$  and  $A = 0.1$ , after the transition point, the film thins at a faster rate than the case of  $A = 0$ . At  $A = 1$ , the formation of the small dimple seems to have little effect on the thinning rate since there is no transition or only a slight transition. The film thins more rapidly with a very small change of thinning rate observed. When the van der Waals forces are strong, as  $A = 10$ , the curve deviates from the  $A = 0$  curve early, indicating faster approach of the drops. No dimple forms to slow down the thinning of the film, so the transition point does not exist in this case.

### 5.3.2 Van der Waals forces calculated from disjoining pressure

Figure 15 shows the evolution of the film between the drops for different values of  $A$ . Like in Fig. 13, rim rupture is observed for  $A = 0.01$ ,  $A = 0.1$  and  $A = 1$ , and nose rupture for  $A = 10$ .

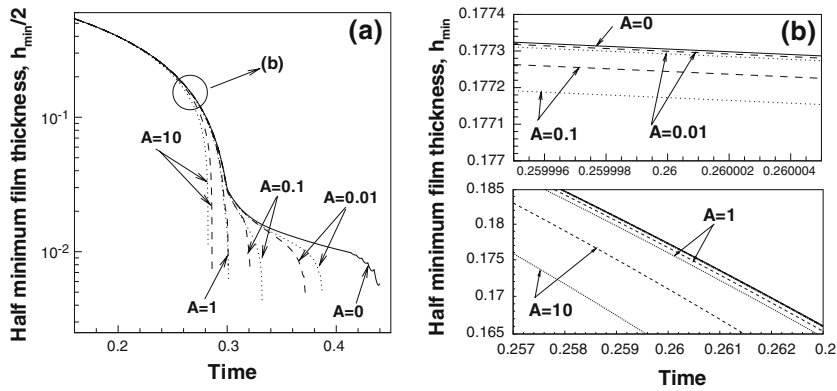


**Fig. 14** Half minimum thickness of the film as a function of time for different values of  $A$ .  $Re = 1$ ,  $We = 1$ ,  $\hat{\rho} = 0.001$ ,  $\hat{\mu} = 0.001$ ,  $142 \times 284$  grid cells. Solid line: van der Waals forces are absent; Dashed lines: van der Waals forces calculated from potential; Dotted lines: van der Waals forces calculated from disjoining pressure

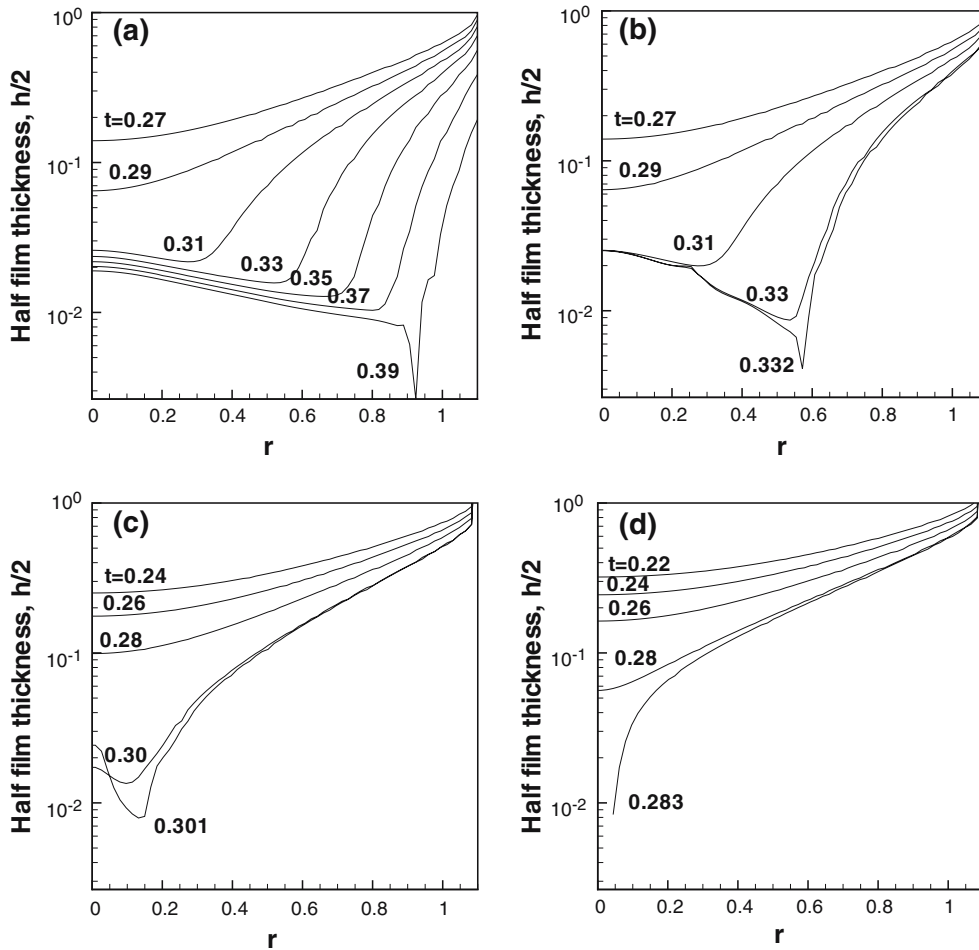


**Fig. 15** Evolution of the film between the drops with van der Waals forces calculated from disjoining pressure.  $Re = 1$ ,  $We = 1$ ,  $\hat{\rho} = 0.001$ ,  $\hat{\mu} = 0.001$ ,  $142 \times 284$  grid cells. (a)  $A = 0.01$ , (b)  $A = 0.1$ , (c)  $A = 1$ , (d)  $A = 10$

Figure 14 compares the curves of half minimum film thickness as a function of time obtained by the two methods and without van der Waals forces. It can be seen from figure (b) that when the separation between the two drops is large, the films thins faster in the disjoining pressure method. The difference between the two methods becomes more obvious as  $A$  increases. However, figure (a) shows that at the later stage of the draining process, at small Hamaker numbers,  $A = 0.01$  and  $A = 0.1$ , the film thins faster in the potential method. As  $A$  increases, this difference between the thinning rate at small separation decreases until  $A = 1$ . When  $A$  becomes 10, the film thins faster in the disjoining pressure method in the entire draining process. This can be explained by the way the disjoining pressure is computed. The form of the disjoining pressure is derived from the interaction potential between two semi-infinite liquid regions separated by a film of uniform thickness. The disjoining pressure is the force one of the regions exerts on a unit area of the other region. In applying this to the interaction of two drops, the assumption that the regions are semi-infinite is valid as long as the drop extent is relatively large, since the potential decreases as  $L^{-6}$ . The assumption that the interface is flat leads to over-prediction of the van der Waals forces and hence of the thinning rate when the interface is convex. The disjoining pressure includes the effect of a flat liquid region, but away from the current grid cell the film thickness is larger if the interface is convex, as it is before the interface flattens. Thus, the disjoining pressure accounts for the attraction of more nearby liquid than is actually present and over-predicts the attractive force. As  $A$  increases, the van der Waals forces become important at a larger separation, so the over-prediction of van der Waals forces has a noticeable effect on the thinning of the film earlier, resulting in more difference from the potential method. On the contrary, when the interface is concave, the disjoining pressure under-predicts the van der Waals forces. This may be the reason why the thinning rate is smaller in the disjoining pressure method than that in the potential method for small Hamaker numbers, because the interface has a concave shape on the two sides of the rim of the dimple, as can be seen from Figs. 13–15.

#### 5.4 Effect of Reynolds number

Figure 16 compares the temporal evolution of the half minimum film thickness for three Reynolds numbers,  $Re = 0.1$ ,  $Re = 1$ , and  $Re = 10$ . There are remarkable differences in the thinning rate of the film. Before the drops are in apparent contact, the gas between the two drops is expelled more slowly as  $Re$  increases. To understand the drop motion at the early stage of the collision, the velocity vectors near the drop at  $t = 0.1$  are shown in Fig. 17. At  $Re = 0.1$ , the velocity inside the drop is nearly vertical, whereas at  $Re = 1$  and  $Re = 10$  the velocity tilts toward the outer boundary. Under such velocities, the drop deforms more at higher  $Re$ . It can also be seen that the velocity at the lower interface of the drops decreases with increasing  $Re$ , which is consistent with the fact illustrated in Fig. 16 that at small times the lower interface moves more slowly at higher  $Re$ . To better understand the velocity field, we subtract the extensional flow to determine how the extensional flow is modified by the presence of the drop. Figure 18 displays this part of the velocity. In the extensional flow a drop tends to be compressed axially. Thus, the curvature, and hence the surface tension force, is elevated along the equator of the drop and decreased at the poles. This leads to the formation of the vortices seen in Fig. 18(a), which tend to restore a spherical drop shape.

As  $Re$  increases, the strength of the two vortices decreases and their positions shift. This is due to the competition between inertial and viscous forces. The clockwise vortex must overcome the downward inertia of the extensional flow. Thus as  $Re$  increases and inertial forces become dominant, the strength and extent of the clockwise vortex decrease. As a result, the extent of the other vortex increases, although its strength decreases as  $Re$  increases. At  $Re = 10$ , the clockwise vortex disappears and the counter-clockwise vortex occupies the whole domain. Finally, we find that as inertia suppresses the vortices, which in turn suppress deformation of the drop, deformation increases. The poles of the drops flatten, so the top of the

**Fig. 16** Half minimum thickness  $h_{\min}/2$  as a function of time for different Re.  $\partial F/\partial z = 0$  boundary condition on the symmetry plane. We = 1,  $\hat{\rho} = 0.001$ ,  $\hat{\mu} = 0.001$ ,  $A = 0.1$ ,  $71 \times 142$  grid cells. Van der Waals forces are calculated by the disjoining pressure method

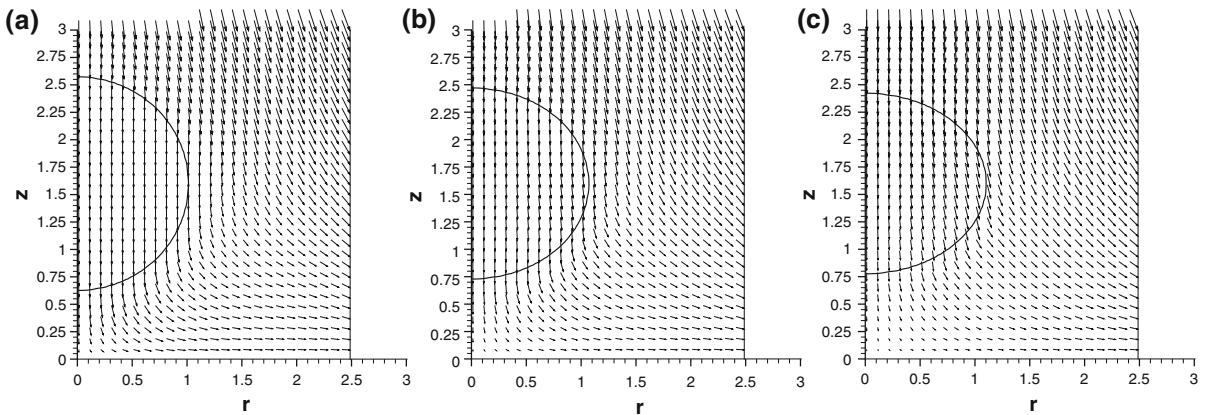
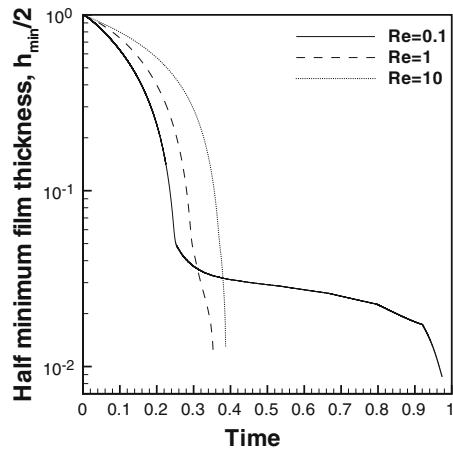


**Fig. 17** Velocity vectors at  $t = 0.1$  for different Re.  $\partial F/\partial z = 0$  boundary condition on the symmetry plane. We = 1,  $\hat{\rho} = 0.001$ ,  $\hat{\mu} = 0.001$ ,  $A = 0.1$ ,  $71 \times 142$  grid cells. Van der Waals forces are calculated by the disjoining pressure method. **(a)** Re=0.1, **(b)** Re = 1, **(c)** Re = 10

drop moves downward faster, and the bottom of the drop moves downward slower as Re increases. Thus in Fig. 16 we see that when the drops are far apart the thinning rate decreases as Re increases.

Figure 19 displays the evolution of film profiles for different Re. As can be seen, a dimple forms in each case, although when the dimple forms the thinning rate changes only slightly or not at all for large Re. After the dimple forms, the film drains more rapidly with increase of Re, according to Fig. 16. While only a moderate increase of thinning rate is observed when Re is increased from 1 to 10, there is a significant increase of thinning rate as Re is increased from 0.1 to 1. This is understandable considering that for higher Re, the effect of drop viscosity is depressed relative to that of drop inertia. Since the viscosity ratio between the gas and the drop fluid is kept constant, the viscous resistance of the gas flow is relatively decreased. Therefore, the film is squeezed out more quickly due to higher impact inertia of the drops and lower resistance force from the gas film.

It should be noted that as shown in Fig. 19, the size of the dimple does not differ significantly between Re = 0.1 and Re = 1, though the thinning rate after the dimple forms is very different in the two cases. This is unlike the results in Sect. 5.3 which show that the thinning rate of the film is closely related to the size of the dimple.

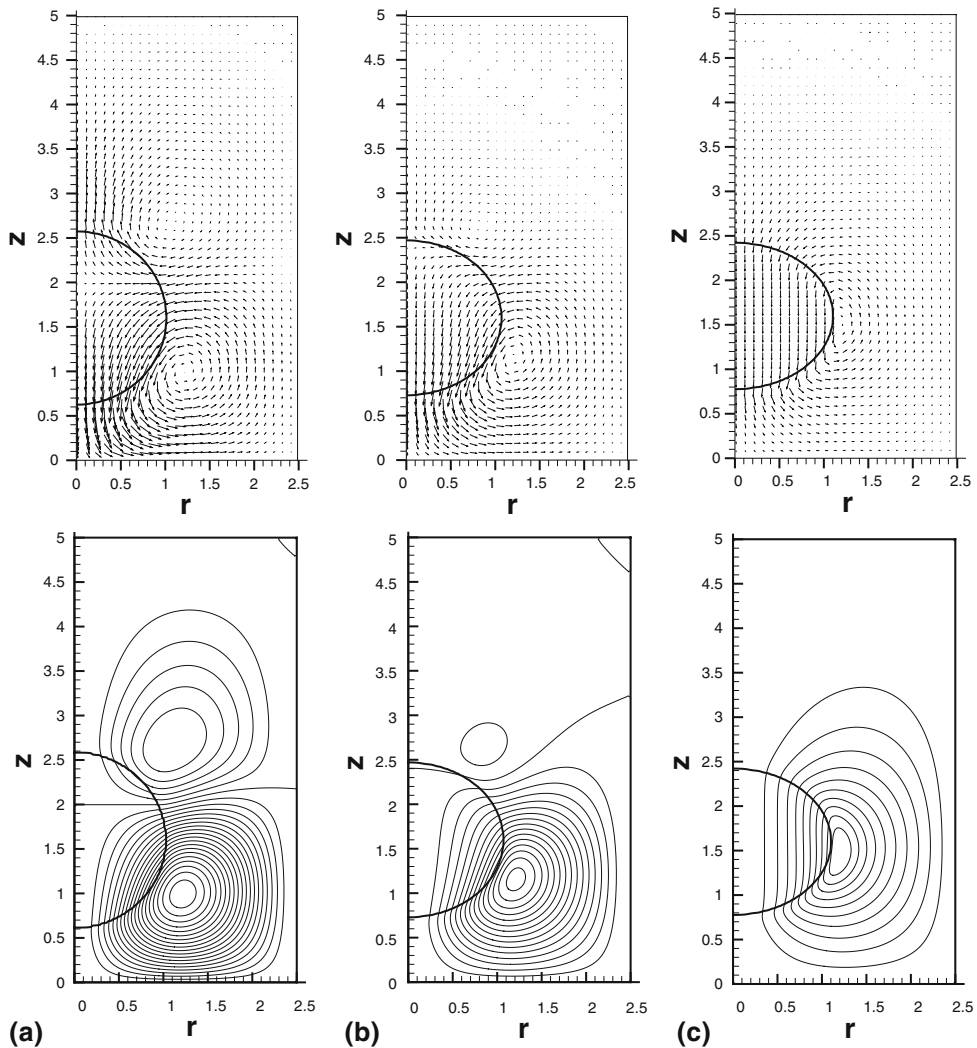


**Fig. 18** Velocity vectors(top) and contours of stream functions(bottom) at  $t = 0.1$  for different  $Re$  for the flow field after the extensional flow is subtracted. The spacing between contours is 0.05.  $\partial F/\partial z = 0$  boundary condition on the symmetry plane.  $We = 1$ ,  $\hat{\rho} = 0.001$ ,  $\hat{\mu} = 0.001$ ,  $A = 0.1$ ,  $71 \times 142$  grid cells. Van der Waals forces are calculated by the disjoining pressure method. **(a)**  $Re = 0.1$ , **(b)**  $Re = 1$ , **(c)**  $Re = 10$

### 5.5 Effect of viscosity ratio

The influence of the viscosity ratio  $\hat{\mu}$  on the thinning rate is shown in Fig. 20. Since other parameters are fixed, increasing  $\hat{\mu}$  means increasing the gas viscosity. Thus the gas in the film exerts higher resistance to the draining of the film. The increasing difficulty of discharging the film results in slower draining rates. A great increase in the thinning rate is observed as  $\hat{\mu}$  is decreased from 0.1 to 0.01. However, as  $\hat{\mu}$  is decreased further, from 0.01 to 0.001, there is only a small increase in the thinning rate, implying an approach to the limit in which the ambient viscosity is zero. The higher resistance from the gas at larger  $\hat{\mu}$  also leads to the increase of the dimple size, as shown in Fig. 21 which depicts the evolution of the film shapes for different  $\hat{\mu}$ .

The flow fields for  $\hat{\mu} = 0.01$  and  $\hat{\mu} = 0.1$  are very similar to that of  $\hat{\mu} = 0.001$  displayed in Figs. 17(b) and Fig. 18(b), so they are not shown.

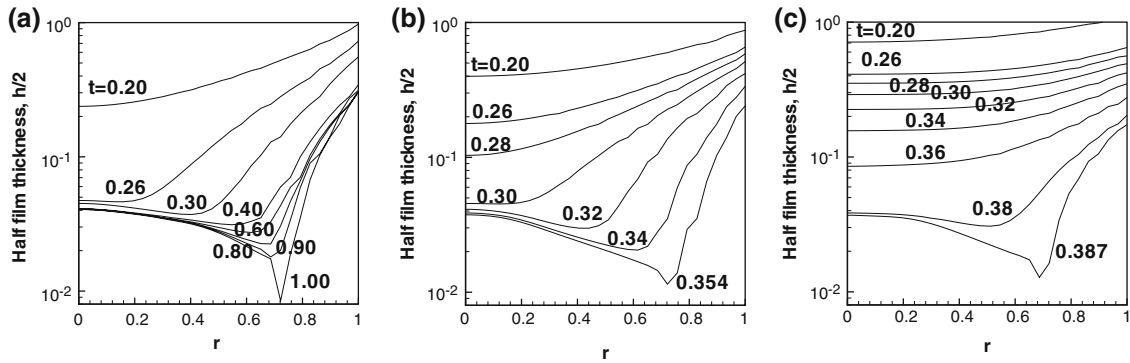
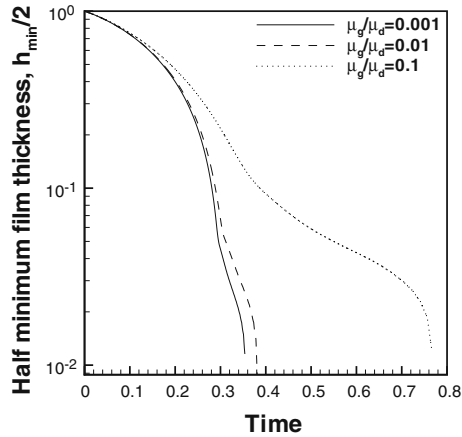


**Fig. 19** Evolution of the film between the drops for different  $Re$ .  $\partial F/\partial z = 0$  boundary condition on the symmetry plane.  $We = 1$ ,  $\hat{\rho} = 0.001$ ,  $\hat{\mu} = 0.001$ ,  $A = 0.1$ ,  $71 \times 142$  grid cells. Van der Waals forces are calculated by the disjoining pressure method. **(a)**  $Re=0.1$ , **(b)**  $Re = 1$ , **(c)**  $Re = 10$

**Fig. 20** Half minimum thickness  $h_{min}/2$  as a function of time for different viscosity ratios.  $\partial F/\partial z = 0$  boundary condition on the symmetry plane.  $Re = 1$ ,  $We = 1$ ,  $\hat{\rho} = 0.001$ ,  $A = 0.1$ ,  $71 \times 142$  grid cells. Van der Waals forces are calculated by the disjoining pressure method



**6 Conclusions**

In this paper the head-on collision of two equal-sized drops in a hyperbolic flow is studied numerically. Both coalescence and bouncing collisions are modeled and the effects of the van der Waals forces on coalescence are investigated. The evolution of the film between the drops is examined.

In our simulations, the two drops interact with each other on the symmetry plane through the volume-fraction boundary condition which consequently affects the collision behavior dramatically. In the standard VOF method, coalescence happens automatically whenever two interfaces come within one grid cell of one other. Our simulations have shown that manipulation of the volume-fraction boundary condition can be used to numerically control coalescence. A symmetry condition leads to coalescence while a zero condition leads to bouncing. In future work we will develop a physical model to properly control the boundary condition.

Two methods have been developed to calculate van der Waals forces. One method incorporates the van der Waals forces in terms of the interaction potential between the two drops. The second method calculates the van der Waals forces from the disjoining pressure in the film between the drops. Results show that the disjoining pressure method over-predicts the van der Waals forces when the interface is convex and under-predicts when the interface is concave. The value of  $A$  for transition from rim to nose rupture lies in the same range in the two methods. The disjoining pressure method is much less computationally intensive,

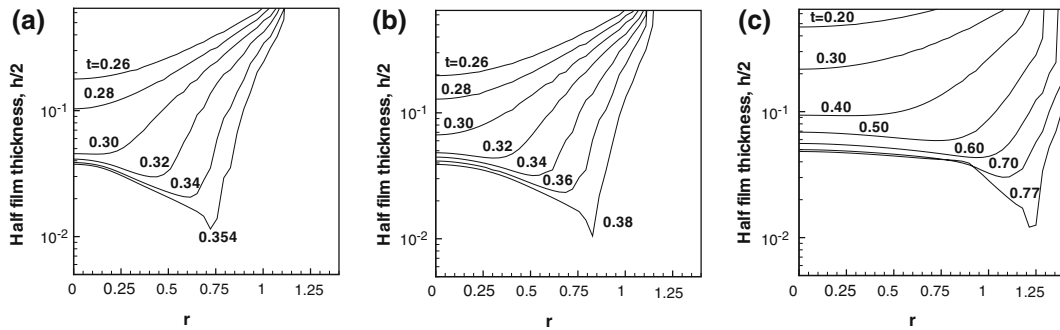


**Fig. 21** Evolution of the film between the drops for different viscosity ratio.  $\partial F/\partial z = 0$  boundary condition on the symmetry plane.  $We = 1$ ,  $Re = 1$ ,  $\hat{\rho} = 0.001$ ,  $A = 0.1$ ,  $71 \times 142$  grid cells. Van der Waals forces are calculated by the disjoining pressure method. **(a)**  $\hat{\mu} = 0.001$ , **(b)**  $\hat{\mu} = 0.01$ , **(c)**  $\hat{\mu} = 0.1$

but relies on the assumption that the interface slope is small. These results show that disjoining pressure method captures the main features of the evolution, but will not provide adequate accuracy under all conditions.

Study of the effect of grid resolution on coalescence shows that in the absence of the van der Waals forces, increase of grid resolution results in increase of coalescence time. In addition, for constant Hamaker number, the effect of van der Waals forces are more apparent with increasing grid resolution.

The influence of Reynolds number and viscosity ratio is also examined. Higher Reynolds number results in larger deformation. Furthermore, the film drainage after apparent contact of the drops is faster for higher Reynolds numbers. The drainage rate differs dramatically between  $Re < 1$  and  $Re > 1$ . In regards to viscosity ratio, larger viscosity ratio leads to slower film drainage.

The suspending fluid is gas whose mean free path of the molecules is about  $0.1 \mu\text{m}$ . The thickness of the gas film between the two drops may become comparable to or smaller than this value. If this happens, the continuum assumption breaks down and the non-continuum effects may become important (36). Furthermore, when the pressure difference across the film driving the film drainage becomes comparable to the ambient pressure, the gas flow in the film will be compressed to such a extent that density change has to be considered (36). However, the non-continuum effects and compressibility are not considered here.

The van der Waals forces take effect over a length scale that is much smaller than the drop radius and result in rapid changes. Therefore, in the near contact area where the length scale is small and changes are fast, a fine grid is a necessity. Whereas away from this region, changes are not that pronounced, so a coarser grid is acceptable. In future work an adaptive mesh will be implemented in the current model so that the thin film between the two drops can be better resolved.

Additionally, in the future more extensive parameter studies and three-dimensional simulations will be performed.

**Acknowledgements** This work was supported in part by the Office of the Vice President for Research and Dean of the Graduate School at the University of Minnesota and by the National Science Foundation under Grant No. CTS-0448078, and utilized the resources of the University of Minnesota Supercomputing Institute. The first author also wants to thank Zonta International for partial support.

## References

- Orme M (1997) Experiments on droplet collisions, bounce, coalescence and disruption. *Prog Energy Combust Sci* 23:65–79
- Ashgriz N, Poo JY (1990) Coalescence and separation in binary collisions of liquid drops. *J Fluid Mech* 221:183–204
- Jiang YJ, Umemura A, Law CK (1992) An experimental investigation on the collision behavior of hydrocarbon droplets. *J Fluid Mech* 234:171–190

4. Qian J, Law CK (1997) Regimes of coalescence and separation in droplet collision. *J Fluid Mech* 331:59–80
5. Leal LG (2004) Fluid induced coalescence of drops in a viscous fluid. *Phys Fluids* 16:1833–1851
6. Foote GB (1975) The water drop rebound problem: dynamics of collision. *J Atmos Sci* 32:390–402
7. Mashayek F, Ashgriz N, Minkowycz WJ, Shotorban B (2003) Coalescence collision of liquid drops. *Int J Heat Mass Transfer* 46:77–89
8. Nobari MR, Jan YJ (1996) Head-on collision of drops –a numerical investigation. *Phys Fluids* 8:29–42
9. Nobari MR, Tryggvason G (1996) Numerical simulations of three-dimensional drop collisions. *AIAA J* 34:750–755
10. Lafaurie B, Zaleski S, Zanetti G (1994) Modeling merging and fragmentation in multiphase flows with surfactant. *J Comp Phys* 113:134–147
11. Premnath KN, Abraham J (2005) Simulations of binary drop collisions with a multiple-relaxation-time lattice-Boltzmann model. *Phys Fluids* 17:122105
12. Pan Y, Suga K (2005) Numerical simulation of binary liquid droplet collision. *Phys Fluids* 17:082105
13. Zinchenko AZ, Rother MA, Davis RH (1997) A novel boundary-integral algorithm for viscous interaction of deformable drops. *Phys Fluids* 9:1493–1511
14. Cristini V, Blawdziewicz J, Loewenberg M (2001) An adaptive mesh algorithm for evolving surfaces: simulation of drop breakup and coalescence. *J Comp Phys* 168:445–463
15. Cristini V, Blawdziewicz J, Loewenberg M (1998) Near-contact motion of surfactant-covered spherical drops. *J Fluid Mech* 366:259–287
16. Ida MP, Miksis MJ (1996) Thin film rupture. *Appl Math Lett* 9:35–40
17. Vaynblat D, Lister JR, Witelski TP (2000) Rupture of thin viscous films by van der Waals forces: evolution and self-similarity. *Phys Fluids* 13:1130–1140
18. Zhang WW, Lister JR (1999) Similarity solutions for van der Waals rupture of a thin film on a solid substrate. *Phys Fluids* 11:2454–2462
19. Chen JD (1985) A model of coalescence between two equal-sized spherical drops or bubbles. *J Colloid Interface Sci* 107:209–220
20. Yiantsios SG, Davis RH (1991) Close approach and deformation of two viscous drops due to gravity and van der Waals forces. *J Colloid Interface Sci* 144:412–433
21. Abid S, Chesters AK (1994) The drainage and rupture of partially-mobile films between colliding drops at constant approach velocity. *Int J Multiphase Flow* 20:613–629
22. Saboni A, Gourdon C, Chesters AK (1995) Drainage and rupture of partially-mobile films during coalescence in liquid-liquid systems under a constant interaction force. *J Colloid Interface Sci* 175:27–35
23. Maldarelli C, Jain RK, Ivanov IB, Ruckenstein E (1980) Stability of symmetric and unsymmetric thin liquid films to short and long wavelength perturbations. *J Colloid Interface Sci* 78:118–143
24. Deryagin BV (1955) Definition of the concept of and magnitude of the disjoining pressure and its role in the statics and kinetics of thin layers of liquids. *Colloid J USSR* 17:191–197
25. Nichols BD, Hirt CW, Hotchkiss RS (1980) Sola-VOF: A solution algorithm for transient fluid flow with multiple free boundaries. Los Alamos National Lab Report LA-8355
26. Hirt CW, Nichols BD (1981) Volume of fluid (VOF) method for the dynamics of free boundaries. *J Comp Phys* 39:201–225
27. Brackbill JU, Kothe DB, Zemach C (1992) A continuum method for modeling surface tension. *J Comp Phys* 100:335–354
28. Harlow FH, Welch JE (1965) Numerical calculations of time dependent viscous incompressible flow of fluid with a free surface. *Phys Fluids* 8:2182–2189
29. James AJ, Smith MK, Glezer A (2003) Vibration induced drop atomization and the numerical simulation of low-frequency single-droplet ejection. *J Fluid Mech* 476:29–62
30. Meijerink JA, Van Der Vorst HA (1981) Guidelines for the usage of incomplete decompositions in solving sets of linear equations as they occur in practical problems. *J Comp Phys* 44:134–155
31. James AJ (2003) Vibration-induced droplet ejection. PhD thesis, Georgia Institute of Technology
32. Tabor D (1991) Gases, liquids and solids and other states of matter. Cambridge University Press, New York
33. Nir S, Vassiliev CS (1988) Van der Waals interactions in thin films. In: Ivanov IB (ed) *Thin liquid films: fundamentals and applications*. Marcel Dekker, New York, pp 207–274
34. Mohamed-Kassim Z, Longmire EK (2004) Drop coalescence through a liquid/liquid interface. *Phys Fluids* 16:2170–2181
35. Rother MA, Zinchenko AZ, Davis RH (1997) Buoyancy-driven coalescence of slightly deformable drops. *J Fluid Mech* 346:117–148
36. Gopinath A, Chen SB, Koch DL (1997) Lubrication flows between spherical particles colliding in a compressible non-continuum gas. *J Fluid Mech* 334:245–269